

Utilizing Conformational Changes for Patterning Thin Films of Recombinant Spider Silk Proteins

Seth L. Young,[†] Maneesh Gupta,[†] Christoph Hanske,[‡] Andreas Fery,[‡] Thomas Scheibel,[§] and Vladimir V. Tsukruk^{*,†}

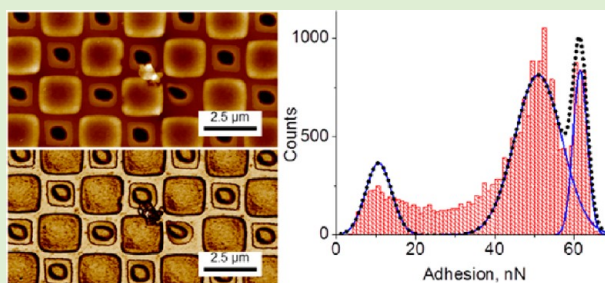
[†]School of Materials Science and Engineering, Georgia Institute of Technology, Atlanta, Georgia 30332, United States

[‡]Physical Chemistry II, University of Bayreuth, Universitätsstrasse 30, 95447 Bayreuth, Germany

[§]Biomaterials, FAN, University of Bayreuth, Universitätsstrasse 30, 95447 Bayreuth, Germany

Supporting Information

ABSTRACT: Recombinant spider silk proteins mimicking the properties of dragline silk proteins represent a class of materials that hold great potential for future high-performance applications. Here we explore the self-assembly behavior of a recombinantly produced spider silk protein based on the dragline silk of the *Araneus diadematus*, eADF4 (C16), by selectively patterning its secondary structure using capillary transfer lithography and solvent-assisted microcontact molding. Two conformational transitions were observed, influenced by initial solvent composition: α -helix/random coil conformation to a more densely packed β -sheet conformation (by casting from 1,1,1,3,3,3-hexafluoro-propanol) and moderate initial β -sheet content to higher β -sheet content (casting from formic acid). Furthermore, by using the solvent-assisted microcontact molding technique, we were able to achieve a submicrometer spatial resolution and reveal fine details of morphological and mechanical changes in patterned regions and at interfaces.



INTRODUCTION

Silk has received much attention in recent years as a promising high-performance, multifunctional material for nanocomposite films, biosensing applications, controlled drug delivery, and tissue engineering, among others.^{1–3} The interest in silk stems from its unique mechanical and viscoelastic properties, having an excellent combination of high strength and high extensibility, as well as its good biocompatibility and mechanical integrity *in vivo*.^{4–21}

Such desirable properties are a result of the proteinaceous nature of the silk molecules.^{1–6,22} In general, the majority of silks contain a large amount of glycine and alanine residues, with some varying amounts of serine, tyrosine, and proline, among others. Each silk molecule is composed of a highly repetitive core sequence of alternating hydrophobic and hydrophilic sequences (comprised of several residues) flanked by nonrepetitive C- and N-termini. Prior to spinning, silk is stored in the gland in very high concentrations: up to 50 w/v %.^{14,23} During spinning, water is removed from the spinning dope as the material is mechanically drawn from the spinneret, inducing protein folding into antiparallel hydrogen-bonded β -sheet crystallites.^{14,24} The result of the silk composition and the complex spinning mechanism employed by the silk-producing organism is a multiphase fibrous material having nanometer-dimension crystallites providing stiffness dispersed in an amorphous matrix, which allows for a viscoelastic response.^{1,25}

Of the different types of silk, the most abundant, and one of the most heavily studied, is that of the domesticated silk worm, *Bombyx mori*, often referred to as silk fibroin (SF). SF is composed of two proteins: a heavy chain (350 kDa) and a light chain (25 kDa), which are linked via a disulfide bond. SF is composed of over 70% glycine and alanine and has repetitive (GAGAGS) motifs, which are responsible for the formation of β -sheet structures. Once processed into an aqueous solution, SF exists in a much more dilute state (less than 10 wt %) in comparison to that found naturally in the silk glands, and its secondary structure takes on a mostly silk I/random coil conformation with helical and β -sheet structures also occurring in relatively low amounts.^{26–28} This random coil state is considered to be highly metastable and can be transformed to the denser, more ordered silk II/ β -sheet state upon exposure to external stimuli including thermal energy, lyotropic salts, mechanical strain, or methanol vapor.²⁷

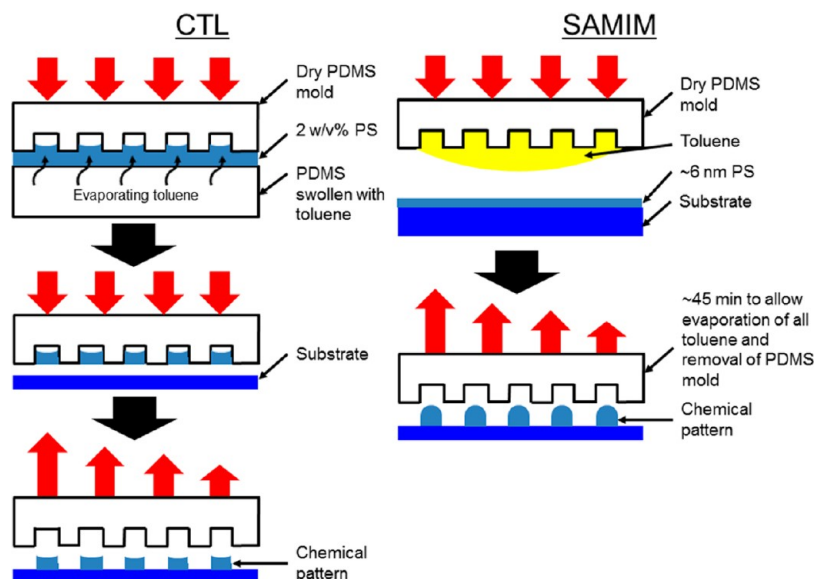
Recently, we have shown that the SF secondary structure, and therefore its mechanical and chemical properties, can be spatially patterned by facile microcontact printing and selective vapor treatment.²⁹ Briefly, a silk film approximately 100 nm thick was cast onto a silicon substrate via spin-assisted self-assembly. By creating a sacrificial polystyrene (PS) mask using

Received: June 23, 2012

Revised: August 24, 2012

Published: September 4, 2012

Scheme 1. Representation of the CTL Technique and the SAMIM Patterning Technique



the capillary transfer lithography technique (see the Experimental Section), these two different conformational states could be reliably patterned with feature sizes down to roughly 1 μm . The conformational patterns were confirmed using confocal Raman microscopy,^{29,30} and atomic force microscopy (AFM) topographic images revealed a distinct difference in surface morphology between the two regions, with the masked regions (i.e., the unexposed regions with a predominantly random coil conformation) showing very smooth morphology, while the exposed regions containing a significantly higher β -sheet concentration displayed a characteristically grainy morphology. Also of note were deep, sharp trenches at the interfacial region between the two areas.²⁹

It is widely accepted that, in nature, the mechanical properties of dragline silks from orb-web-weaving spiders are superior to the silk from the cocoon of *B. mori*. However, due to the predatory, and sometimes cannibalistic, nature of spiders and the low yields of silk that could potentially be harvested from a spider web, natural spider silks do not represent a commercially viable option for engineered silk materials in larger quantities; thus there has been a strong effort to develop biotechnologically produced synthetic proteins that mimic dragline silk.^{1,14,15,31–33}

One such effort, undertaken by Scheibel's group, has resulted in the development of so-called C16, which is derived from the dragline silk protein ADF-4 from the European garden spider, *Araneus diadematus*.³⁴ C16 is recombinantly produced in *Escherichia coli*, and has the chemical structure (GSSAAAAAASGPGGYGPENQGGYGPGGP)₁₆.^{31,34} C16, like many natural dragline silk proteins, consists primarily of glycine and alanine residues, with (A)_n ($n = 8$ for C16, $n = 4–12$ for natural dragline silk molecules) stretches serving as the primary crystallizable motif.^{32,34,35} C16 can be easily processed from solution, allowing the formation of complex morphologies, such as hydrogels, microspheres, microcapsules, and thin films.^{13,34} The secondary structure of C16 can be influenced by the solvent in which it is dissolved. Fluorinated solvents such as 1,1,1,3,3,3-hexafluoro-propanol (HFIP) are known to promote α -helical formation in denatured proteins,³⁶ and this is indeed the case for C16 dissolved in HFIP. Attempts

to utilize secondary structure transformations from a random coil/ α -helical state to a β -sheet state in recombinant spider silk proteins for controlled patterning of materials properties with high spatial resolution in thin films have not been reported to date.

Here, we demonstrate high-resolution patterning of the secondary structure in C16 cast from different solvents: HFIP (induces initial α -helix content) and formic acid (FA; induces initial β -sheet content). We also exploit a patterning technique that allows for smaller pattern feature sizes, reduced from a 1 μm limit reported in our previous study²⁹ to a sub-micrometer scale (specifically, about 300 nm). Precise spatial control over the secondary structure of protein films with high precision, and therefore their chemical and mechanical properties, provides a starting point for the development of many practical biotechnology approaches, including selective cell growth scaffolds, robust and tough nanocomposites, and sensing devices among others.

EXPERIMENTAL SECTION

Sample Preparation. The recombinant spider silk protein eADF4 (C16) was produced and purified as described previously.³⁴ Briefly, transformed cells (*E. coli* strain HMS174[DE3]) were grown at 37 °C in LB medium to an OD₆₀₀ of 0.5. Before induction with 1 mM isopropyl- β -D-thiogalactosid (IPTG), cells were shifted to 25 °C. Cells were harvested after 3–4 h of induction. After cell disruption and removal of cell debris, the supernatant was incubated at 70 °C to precipitate bacterial proteins, followed by an ammonium sulfate precipitation to precipitate eADF4 (C16), which was stored after lyophilization.

C16 solutions (2 mg/mL) were prepared by gentle shaking overnight in either FA (85%) or HFIP (99%). Silicon wafers were cleaned in piranha solution (3:1 mixture H₂SO₄:H₂O₂) for 1 h and subsequently rinsed thoroughly with 18.2 Ω -cm resistivity Nanopure water, obtained from a Barnstead Nanopure system. 50–70 nm thin C16 films were fabricated by spin-coating onto the clean silicon substrates at 3000 rpm. It is worth noting that the solvents do have the ability to degrade the protein, but only after many days.³⁷ There are many examples in the literature of silk solutions cast from both FA and HFIP.^{38–41} Here, only small amounts of solution were made (1 mL at a time), and the films were cast typically the day after dissolution, and a fresh solution was made for each casting.

To pattern the C16 films, two methods were used: capillary transfer lithography (CTL)⁴² and solvent-assisted microcontact molding (SAMIM) (both shown in Scheme 1).^{43,44} For CTL, a poly-(dimethylsiloxane) (PDMS) substrate was swollen by sonication in toluene for 2 min. PS solution was then applied to the PDMS substrate (PS, 2 w/v% in toluene, 200 kDa MW) and spin-cast at 3000 rpm, resulting in a film with a thickness of approximately 150 nm. A patterned PDMS mold was then brought into conformal contact with the PS film on the PDMS substrate, and pressure was applied for 1 min, causing the PS to become entrapped in the recessed regions of the mold. The PDMS mold and entrapped PS pattern were then slowly removed from the substrate and immediately transferred onto the spin-coated C16 films by application of pressure for 1 min. During the application of pressure, the PS adheres onto the C16 film such that, upon removal of the PDMS mold, the PS pattern remains on the surface of the C16 film.

To produce a true chemical pattern via the SAMIM technique, 0.2 w/v% PS was spin-coated at 3000 rpm onto a C16 film, resulting in a PS film with a thickness of 6 nm, as measured by AFM scratch tests and confirmed via ellipsometry. A small droplet of toluene was placed on a patterned PDMS mold, and this was brought into conformal contact with the 6 nm PS film, with the only applied pressure being a result of the weight of the PDMS mold. The mold was allowed to stand for 45–60 min to ensure that all toluene had completely evaporated and then removed, leaving behind a patterned PS region on the surface of the C16 film.

To induce protein conformational changes, the masked C16 films were exposed to MeOH vapor. MeOH vapor was formed by placing MeOH in a glass Petri dish and then heating to 40 °C on a hot plate. The masked films were then suspended above the liquid and exposed to the vapor for roughly 20 s, changing the protein conformation in the unmasked areas. After drying with nitrogen and allowing to stand in ambient conditions for several minutes, the PS mask was removed by immersing in toluene for approximately 5–10 s, leaving a protein film having a spatially patterned secondary structure. Residual toluene was removed, and the patterned C16 films were dried with nitrogen.

Characterization. AFM measurements were made on a Bruker Icon microscope using peak force tapping (PFT) mode.⁴⁵ In PFT mode, a set point force (typically a few nanoNewtons) is established by the user such that the sample is deformed by approximately 2–5 nm and the cantilever deflection versus z-position in retracting mode is monitored and analyzed in real time, using the Derjaguin–Muller–Toporov (DMT)⁴⁶ model of elastic contact to determine the apparent elastic modulus with a lateral resolution that is comparable to the tip radius (below 10 nm) and the stress field beneath the sample surface induced by applied pressure from the tip. Although the absolute values of the apparent elastic moduli measured here can be significantly affected by a combination of plastic deformation, adhesive interactions, and relaxation processes, the “instant” distribution of relative values reflect the surface distribution of the local mechanical properties.⁴⁷ Other mechanical properties that are evaluated in real time are the adhesive forces and energy dissipation. PFT modulus measurements were made with Bruker’s RTESPA cantilevers, which have a tip radius of approximately 10 nm and typical spring constant values ranging from 20 to 30 N/m. To enhance the adhesive interactions between the AFM tip and the patterned C16 films, Bruker’s ScanAsyst tips were used, which have spring constants that typically range from 0.4 to 0.7 N/m. It should be noted that the height images presented in this paper were obtained using the ScanAsyst tips with low spring constant (0.4 N/m). The silk films are generally very stiff under these conditions; adhesive forces alone would produce negligible effects on the height measurements.

Silk secondary structure was monitored via FTIR using a Bruker Vertex 70 FTIR Spectrometer with a Harrick Twin Parallel Mirror Reflectance Attachment.¹⁸ Silk films were cast onto a silicon multireflection crystal, and ATR-FTIR absorbance spectra were taken at a resolution of 1 cm⁻¹ both before and after exposure to methanol to confirm conformational changes. The sample chamber was purged with nitrogen for several hours before measurements were taken, and spectra were compensated for atmospheric water and

carbon dioxide using the atmospheric compensation function in OPUS version 6 Spectroscopy Software.

RESULTS/DISCUSSION

After spin-casting, the surface morphology of the C16 films was investigated using AFM (Figure 1). Topographic images for

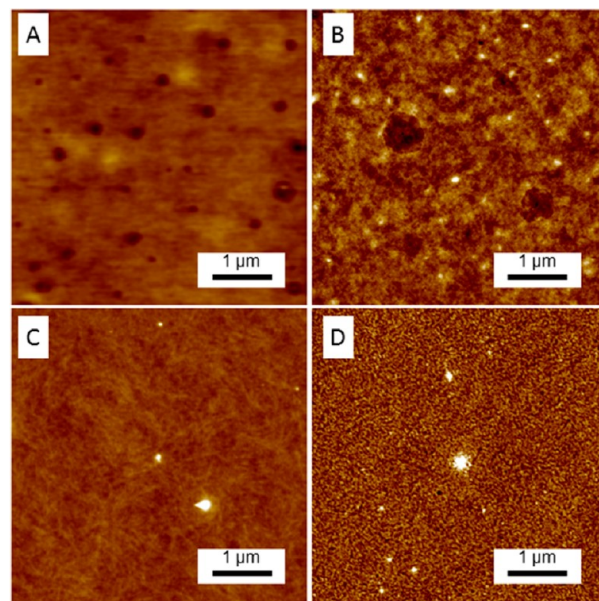


Figure 1. AFM images showing the morphology of C16 films cast from HFIP (A), cast from HFIP and then exposed to MeOH vapor (B), cast from FA (C), and cast from FA and exposed to MeOH vapor (D). Z scales: 10 nm (A,B), 4 nm (C,D).

C16 cast from HFIP show a multi scale structure (Figure 1A,B). On the microscale, a wavy morphology is observed uniformly across the entire film. On the nanoscale, the film is smooth with a uniform distribution of pinholes formed as a result of inhomogeneous solvent evaporation. Because of the dimensions of the AFM tip and the film, we were not able to absolutely confirm whether the pinholes protruded all the way through the film. After exposure to MeOH vapor, resulting in increasing β -sheet content, a vast majority of the pinholes disappeared, while the remaining ones seemed to have some material removed in the area immediately surrounding them (resembling a “strip-mine” or “surface-mine”). There was an apparent increase in surface roughness and the addition of nanometer-sized bumps; however, the characteristic grainy morphology was not observed in this case. C16 films cast from FA show a similar morphology to that of regenerated SF (Figure 1C,D), with a very smooth surface having occasional nanometer-sized bumps which are very sparsely distributed. Upon exposure to MeOH vapor, the film showed increased surface microroughness and took on the typical grainy microstructure often seen in silk films.

The planar C16 films were also studied via ATR-FTIR both before and after MeOH vapor exposure to confirm that a conformational transition had taken place. Briefly, each solution was cast onto a multireflection ATR crystal, and 100 FTIR spectra were taken, coadded, and averaged, and the amide I band (1600–1720 cm⁻¹) was monitored. A characteristic peak shift was observed, indicating significant changes in the secondary structure of the protein film (Figure 2).^{30,48}

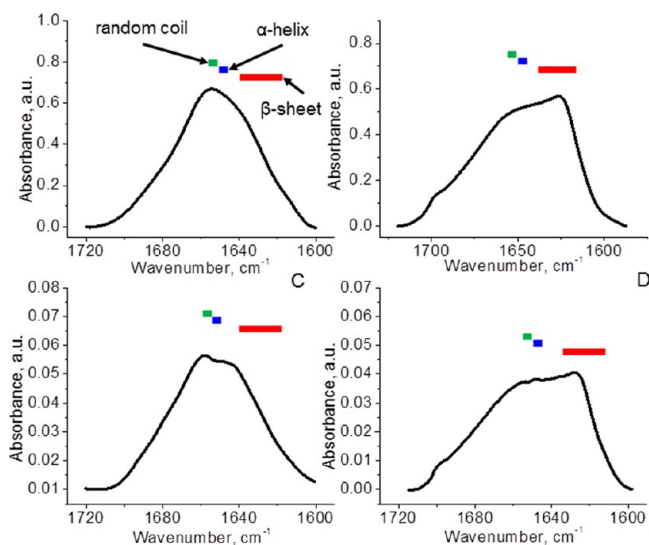


Figure 2. ATR-FTIR spectra of C16 cast from HFIP: as-cast (A) and after methanol treatment (B). ATR-FTIR spectra of C16 cast from FA: as-cast (C) and after methanol treatment (D). Bars above each spectrum represent the approximate position of the absorbance bands for each structural feature.

The thickness of the cast films was observed and recorded using the AFM scratch test,⁴⁰ and these results were confirmed via ellipsometry. Figure 3 shows the AFM height images superimposed with a representative cross-sectional profile constructed by averaging 20 horizontal lines obtained from the image. Because the micrometer-scale waviness in the films cast from HFIP hinders easy visualization of average film thickness, height distributions were also taken and fitted with Gaussian curves to determine the average film thickness. C16 films cast from HFIP were observed to have an average as-cast thickness of 61 nm (A,C) and a MeOH-treated thickness of 53 nm (B,D), representing a 13% decrease in film volume. This is a result of the β -sheet crystallites being in a denser conformation than the α -helical or random coil structures. Also, a volume reduction should be expected because the pinholes, which were originally present, have been “filled in” due to molecular rearrangements. This volume reduction seems to have an adverse effect on the morphology of patterned films, resulting in a significant amount of film tearing (as discussed below). Here, the porous structure and the aforementioned wavy-like structure are readily apparent in the significant broadening of the film peaks located at 53 and 61 nm.

Also seen in Figure 3 are the AFM height images and the height distributions from scratched C16 films cast from FA.

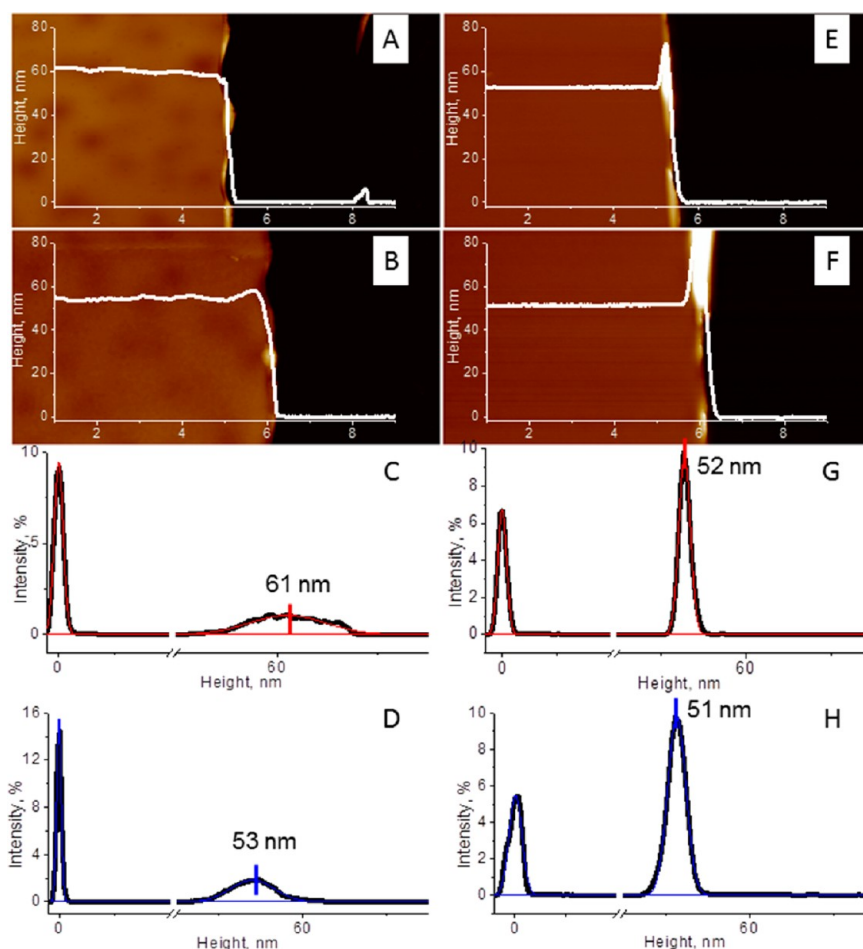


Figure 3. Height images of scratch tests performed on C16 cast from HFIP (A) and exposed to methanol (B), and height distribution profiles of C16 cast from HFIP (C) and exposed to methanol (D). Height images of scratch tests performed on C16 cast from FA (E) and exposed to methanol (F), and height distribution profiles of C16 cast from FA (G) and exposed to methanol (H). Superimposed over the AFM height maps are representative cross sections produced by averaging 20 horizontal scan lines in the image. Z scale: 150 nm.

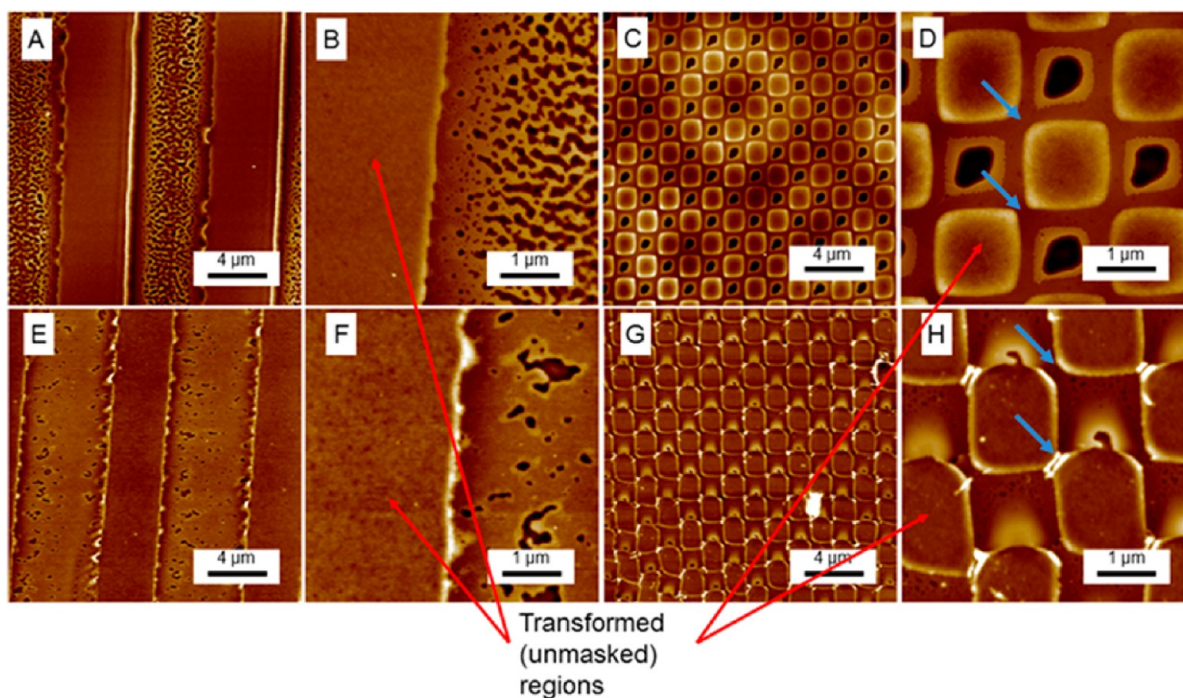


Figure 4. AFM topographical images of patterned C16 cast from HFIP: (A,B) line pattern with a $10\ \mu\text{m}$ periodicity, (C,D) square pattern with dimensions of approximately $1.5\ \mu\text{m} \times 1.5\ \mu\text{m}$. Z scale: 60 nm. AFM topographical images of patterned C16 cast from FA: (E,F) Line pattern with a $10\ \mu\text{m}$ periodicity, (G,H) square pattern with dimensions of approximately $1.5\ \mu\text{m} \times 1.5\ \mu\text{m}$. Blue arrows indicate where the interconnecting PS struts existed on the original mask. Z scale: 40 nm.

Here, the distribution peaks are sharp, representing a very flat, uniform film with no secondary wavy morphology. The observed thickness of the as-cast film was 52 nm (E,G) while the treated film appeared to have a thickness of 51 nm (F,H), suggesting very little volumetric change during secondary structure transformations. This is expected, however, since the secondary structure initially present in the as-cast film contained some β -sheet content, and the methanol treatment simply increased the β -sheet content.

Figure 4 shows patterned C16 films cast from HFIP (A–D) and FA (E–H). The patterned regions are formed when a solvent-induced conformational transition occurs in the regions that are not blocked by the PS mask that was deposited via CTL or SAMIM prior to solvent treatment. Therefore, periodic patterns are created in which the secondary structure of C16 proteins in the masked regions is either in an α -helical/random coil conformation (HFIP) or has low initial β -sheet content (FA), while the unmasked regions take on an enhanced β -sheet conformation. Figure 4A,B,E,F shows a line pattern with a $10\ \mu\text{m}$ periodicity fabricated via CTL, with red arrows indicating the areas that have undergone transformation. We expect that these regions have undergone transformation because the line pattern periodicity is asymmetric. That is to say, the PDMS mold was cast from a master, which was a silicon wafer with $3\ \mu\text{m}$ -wide rectangular trenches micromachined into it to a uniform depth of approximately $1.5\ \mu\text{m}$, each separated by a distance of $7\ \mu\text{m}$. Curing PDMS over such a master would result in the reverse, or negative, of this pattern, and finally employing the CTL process as described above would result in $7\ \mu\text{m}$ PS lines separated by a distance of $3\ \mu\text{m}$.

Figure 4C,D,G,H shows a square lattice pattern with dimensions of approximately $1.5\ \mu\text{m} \times 1.5\ \mu\text{m}$ with red arrows pointing to what is the transformed region. The square pattern produced by CTL is unambiguous, facilitating the recognition

of the transformed and untransformed regions. In this case, the transferred PS pattern has square structures, typically around $1\ \mu\text{m}$ in height, which are interconnected at their corners via $400\ \text{nm}$ diameter struts. The areas where these struts were located on the PS during MeOH exposure are easily visible in Figure 4.

Readily apparent in the patterned C16 films is the large amount of tearing in the untransformed, or masked, regions. In our recent study with SF, the only observed tearing occurred at the interfacial area between the transformed and untransformed regions. This was postulated to be due to the as-cast film being held firmly in place by the PS mask and the silicon substrate, while the unmasked regions experienced a decrease in volume as a result of the formation of β -sheet crystallites, which are denser than the random coil structure of the masked areas. Ultimately, the silk II regions with microscopic lateral dimensions pull away from the masked random coil regions forming the trench, which had a width that was less than $100\ \text{nm}$.²⁹ Facilitating this phenomenon is the fact that the denatured SF occurring in regenerated aqueous solutions is not monodisperse, as it is formed from two different proteins. C16, on the other hand, is a purified, monodisperse protein,³⁴ and hence the interfacial region between the masked and unmasked regions is stronger, causing stresses to be distributed over a larger area rather than right at the interface. Such a redistribution results in the absence of the sharp and deep trenches that were observed earlier for SF films.²⁹

Close inspection of Figure 4A,B reveals tearing that is oriented primarily in the x -direction (from left to right in the image). These tears show widths that range from approximately $90\ \text{nm}$ up to $125\ \text{nm}$. In comparison, the pinholes observed in the as-cast film (Figure 1) have diameters that range from 225 to $250\ \text{nm}$. This suggests that, upon transformation, stress buildup from the volume decrease associated with the transition from α -helical/random coil conformation to β -sheet con-

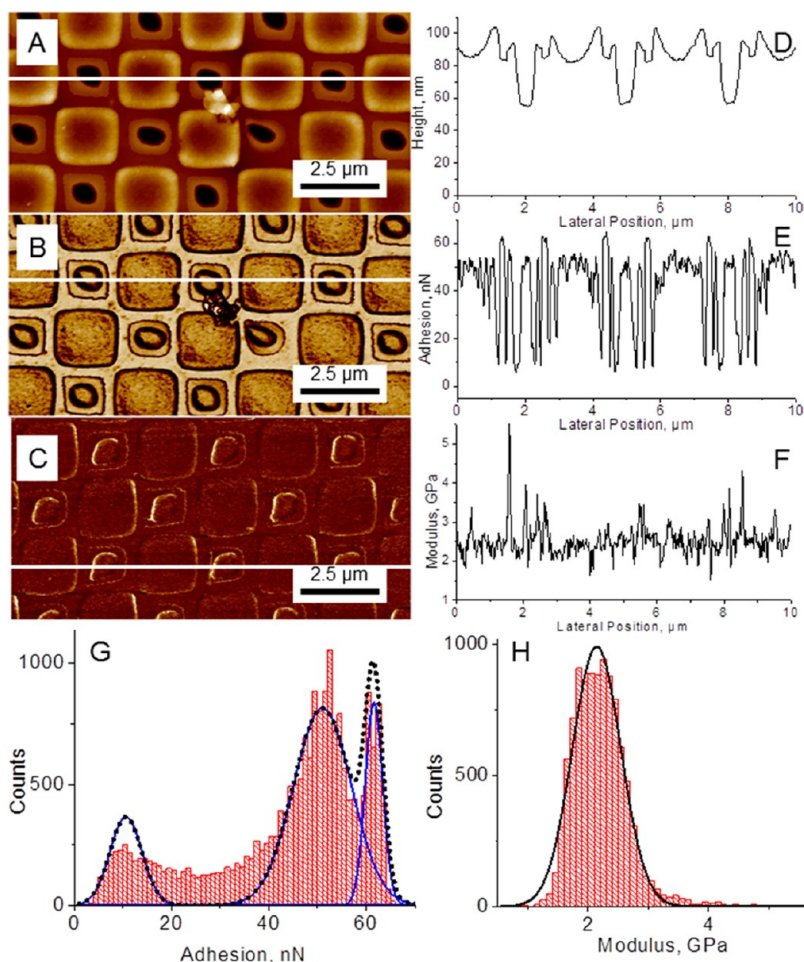


Figure 5. C16 cast from HFIP patterned with a square lattice. (A) Topography, (B) adhesion map, (C) modulus map. Representative cross sections: height (D), adhesion (E), and modulus (F). Histograms depicting the distribution of adhesion (G) and modulus (H) overlaid with Gaussian fits. Z scales: 70 nm, 75 nN, 5 GPa.

formation causes these pinholes to be strained in the direction of stress (perpendicular to the lines), possibly causing multiple strained pinholes to intersect and combine. It is interesting that many of these tears are oriented primarily horizontally because materials typically fail in a direction perpendicular to applied stress⁴⁹ (in the direction of the lines and down into the film thickness), possibly indicating increased plasticity in the untreated regions. Indeed, such increased plasticity in C16 films cast from HFIP has previously been noted. This behavior is attributable to a lower content of stiff β -sheets, and the unraveling and extension of protein chains after hydrogen bonds in the amorphous regions are broken upon stretching.⁵⁰

In contrast to the line pattern, the square pattern shows one large tear (Figure 4C,D). The key difference here is the application of biaxial stress, possibly resulting in a massive buildup of strained pinholes that ultimately deform into one large hole. Also of note is the raised region that appears around the rim of these holes, which we suspect may contain a significant β -sheet content. While it has previously been observed in C16 films that the influence of residual HFIP molecules hindered the formation of β -sheet structures on stretching,⁴⁶ the spin-casting process could have resulted in a gradient of residual HFIP molecules trapped in the film. Additionally, at the surface is the presence of the hydrophobic PS mask, which would give hydrophobic β -sheet structures a

site to segregate to, facilitating the formation of β -sheet structures during stretching.

Therefore, it is entirely possible that the raised region has undergone a shear-induced transformation. Supporting this is adhesion mapping of this pattern, which revealed a slightly lower adhesive interaction with the hydrophilic AFM tip in the raised regions around the tear and at the bottom of the tear than with the flat, untransformed regions between the tear and the transformed regions (discussed below).

Not surprisingly, the tearing observed for the line patterns for C16 cast from FA (Figure 4E,F) is far less significant than that observed for films cast from HFIP. This comes as a result of the inclusion of initial β -sheet content, serving to stiffen the film and increasing its resistance to deformation. Additionally, the transformation here primarily involves an increase in β -sheet content, rather than α -helix to β -sheet conformational transition, such that the volume change is far less than that observed in films cast from HFIP, applying a lower stress to the masked regions upon post-treatment. The cracks on the untransformed regions on this film appear to be mostly to one side, likely due to a MeOH exposure gradient during post-treatment occurring when the films are lowered to the Petri dish containing liquid MeOH at a slight angle. It should be noted that the evenly distributed tearing observed in films cast from HFIP does not necessarily mean that they were exposed completely uniformly, but rather points to the enhanced

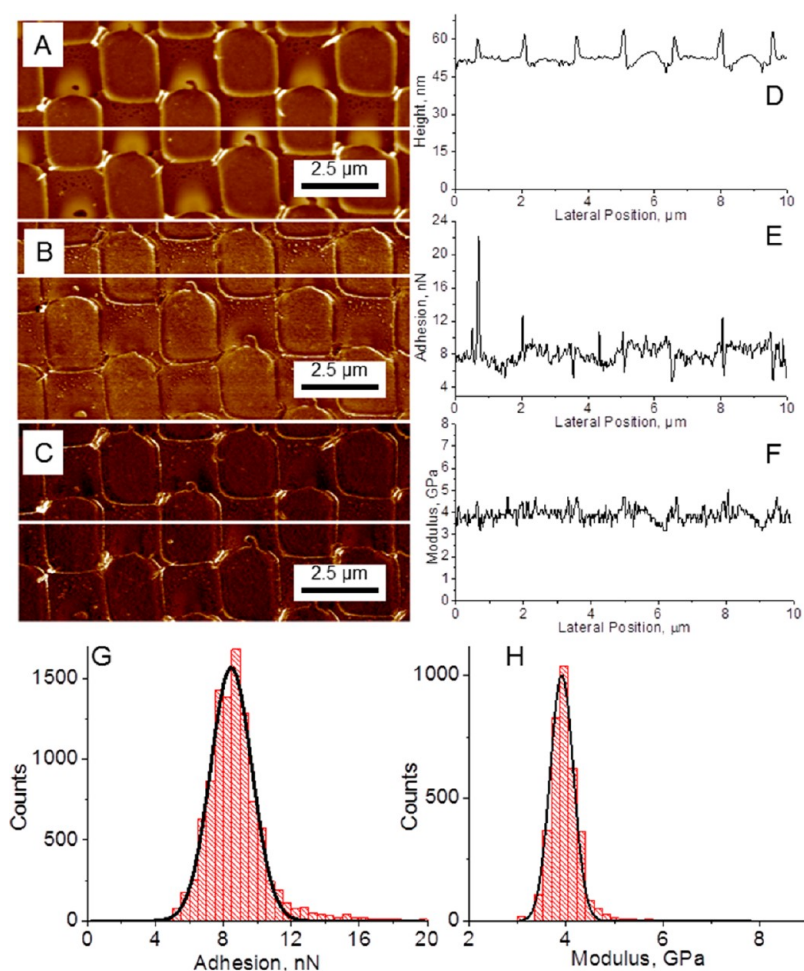


Figure 6. C16 cast from FA patterned with a square lattice. (A) Topography, (B) adhesion map, (C) modulus map. Representative cross sections: height (D), adhesion (E), and modulus (F). Histograms depicting the distribution of adhesion (G) and modulus (H) overlaid with Gaussian fits. Z scales: 50 nm, 20 nN, 15 GPa.

plasticity of C16 films cast from HFIP allowing for some dissipation of stresses through deformation. The asymmetric tearing seen in the patterned films cast from FA occurs most likely because of their inherently lower flexibility, which due to the initial β -sheet structures acting as physical cross-links and not allowing for as much stress relaxation via plastic deformation as observed in patterned films cast from HFIP.⁴⁶ A similar result is observed for the square pattern for the C16 films cast from FA.

A common feature in all of the patterned films is the occurrence of a raised area at the edge of the transformed regions. Originally, we expected a rather smooth transition between the two regions, and to some extent this is what we have gotten, as there is no tearing at the interface as was observed with SF, suggesting a much stronger interaction among the monodisperse C16 molecules. On the basis of the scratch tests, one would expect that a film contraction upon post-treatment with MeOH would result in, if anything, tearing at the interfacial regions of the patterns. However, simply looking at the before and after states of the transition can be somewhat misleading. While it is difficult to directly observe conformational transitions of protein molecules since they occur so rapidly,⁵¹ many theoretical models suggest that the metastable intermediate state between the two stable conformations is that of an unfolded protein.^{47,52–54} Therefore,

when the MeOH vapor penetrates the film thickness swelling occurs, allowing the α -helices present in both films to unravel into a more random coil-like state. The unraveled proteins then quickly refold into β -sheet structures. This relaxation could possibly help to explain why a raised bump is seen in the transformed regions at the interface. Considering that the PS features are stiff and much more massive compared to the thickness of the film, a volume increase in the underlying C16 film would cause a small expansion, resulting in the film swelling up between the PS structures. This combined with a quick contraction would then cause a stress buildup at the edges, causing the transformed regions to buckle in this area. Interestingly, the raised regions at the interface of the films cast from HFIP are higher than the ones from the C16 films cast from FA. This could be influenced by the higher stiffness of the films cast from FA, but also these films have less α -helical structures to unravel, implying less volumetric change and a lower stress buildup at the edge of the PS structures.

Micromapping analysis of the square pattern for films cast from HFIP revealed a significant contrast in the adhesion of the two different regions. Figure 5 shows the height image (A), adhesion map (B), and the histogram of adhesive forces overlaid with a Gaussian fit (D). The data analysis shows that the AFM adhesion map and the adhesion histogram display an unusual trimodal distribution of adhesive properties. According

to the histograms, the untransformed regions have a nominal adhesion force to the tip of 62 nN, whereas the adhesive forces are reduced by 15% for transformed regions. This is the expected result as the exposure to methanol causes hydrophobic β -sheets to separate to the silk–air interface, and the silicon probe, which has a thin native oxide layer, would adhere more favorably to the hydrophilic, untransformed regions than the hydrophobic, transformed regions. The interfacial regions showed a lower adhesion due to topographical effects (ridges). By contrast, no significant changes in the apparent modulus are observed between the masked and unmasked regions of the C16 film cast from HFIP. Figure 5C shows the modulus map, which is complemented by the modulus distribution overlaid with a Gaussian fit (H). As can be seen, the apparent modulus of the film is just above 2 GPa and appears to be quite uniform, with some bright regions appearing at the interfacial regions due to topographical contribution into the contact area. It is unclear why there is no shift in the elastic modulus of the two regions, but it may be a result of the data collection method, wherein force curves are taken at 2 kHz, which may enhance the apparent stiffness of the untransformed region, which already has an elastic modulus close to that of the transformed regions.⁴⁶

Figure 6 shows the height image, modulus map, and adhesion map, as well as representative cross sections and modulus and adhesion histograms fitted with a Gaussian curve for a C16 film cast from FA and patterned using the square lattice. Patterned films cast from FA reveal little difference in the adhesive forces in masked and unmasked regions. This is a result of the initial β -sheet content in the as-cast film. The as-cast film most likely has some significant content of hydrophobic β -sheet crystallites at the surface. As a result, the AFM probe essentially sees the same surface in the two regions. As can be seen in the adhesion cross-section (Figure 6E), there is some periodic modulation of adhesive forces; however, it is hard to say whether this is a true feature of the two different phases because the untransformed regions have a complex morphology that could easily affect the measurement. No clear differences in elastic modulus of the patterned films cast from FA were observed, due to the similar structural features in the film before and after MeOH treatment, and the speed at which the measurements have been taken.

To create a mold for submicrometer patterns, PDMS was cast over a substrate fabricated via interference lithography that contained ridges that are roughly 300 nm wide separated by 300 nm. According to the cross-section of the AFM height image of the PDMS mold used for SAMIM (provided in the Supporting Information), after the SAMIM process, one would expect to see lines with a diameter of 400 nm separated by 350 nm. It is worth noting, however, that because PDMS is a very compliant material, simply adding additional pressure to the back of the mold during SAMIM can vary the width of the lines (or vice versa if pressure on the mold is decreased; Supporting Information).

Indeed, SAMIM using PS on C16 films resulted in large areas of uniform PS lines with diameters of approximately 400 nm separated by 300 nm (shown in Figure 7). Figure 7C shows a three-dimensional (3D) height representation of a patterned C16 film. Here the color does not correspond to height, but rather to the mechanical energy dissipation of the AFM tip. Because the PS and C16 have different mechanical and chemical properties, the energy dissipated by the two is different. In Figure 7C there is a clear, sharp interface between

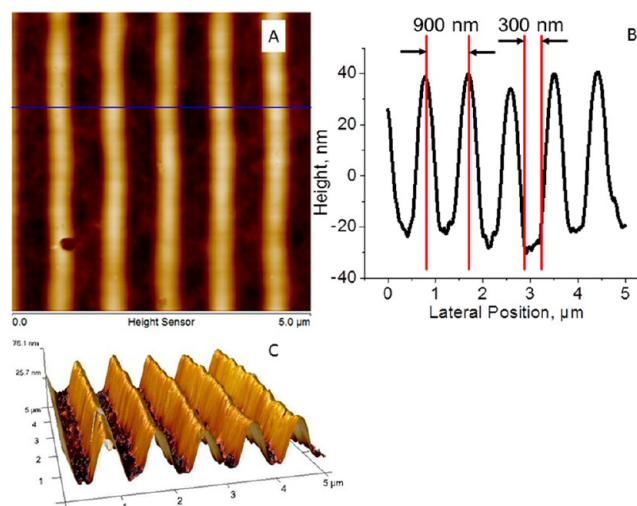


Figure 7. (A) AFM height image of a C16 film cast from FA and patterned using the SAMIM method. (B) Cross-sectional profile of the line indicated in A. (C) 3D height image of the pattern with the color representing energy dissipation.

the PS lines and the C16 film, suggesting that the SAMIM method did in fact produce a true chemical pattern, rather than a physical pattern.

Figure 8 shows the C16 films patterned using the SAMIM technique. Here, films cast from HFIP and films cast from FA look strikingly similar. In each, there is a raised region of approximately 20 nm, with the edges of these regions typically flaring up several nanometers higher than the center. We postulate that the raised regions are the transformed regions. This would agree with the suggestions put forth earlier in this article about the behavior of these films. However, since the patterned lines in this case are much smaller than the 7 and 1.5 μm regions presented above, it appears as though we have unintentionally pushed the edges of the raised regions together. Cross-sectional analysis (Figure 4S, Supporting Information) also reveals that the untransformed areas (originally masked by PS with a diameter of 400 nm) have decreased to a width of approximately 210 nm, while the transformed regions (originally the 300 nm space) have increased to approximately 480 nm. This difference could easily be a result of the more significant role solvent undercutting would play in the smaller features sizes, and the size of the PS mask itself, with the smaller lines being more easily deformed by the stress buildup due to swelling. Whereas the PS features in the larger, CTL patterns are massive (roughly 1–1.5 μm in height) compared to the film thickness, the PS lines created by SAMIM begin to approach the thickness of the as-cast film (~ 300 nm wide and ~ 100 nm height). In this case it may be possible that the stress buildups associated with the conformational changes are enough to deform and move the smaller PS lines. In fact, if a volumetric increase does occur during transformation, then the reduced area for it to occur through (300 nm spaces) would result in higher stress buildup in general. This may explain why the raised region for both films cast from HFIP and FA appear to be approximately the same height as for the SAMIM pattern, whereas the larger area for expansion, contraction, and relaxation in the CTL patterns resulted in a smaller interfacial bump in films cast from FA in comparison to those cast from HFIP.

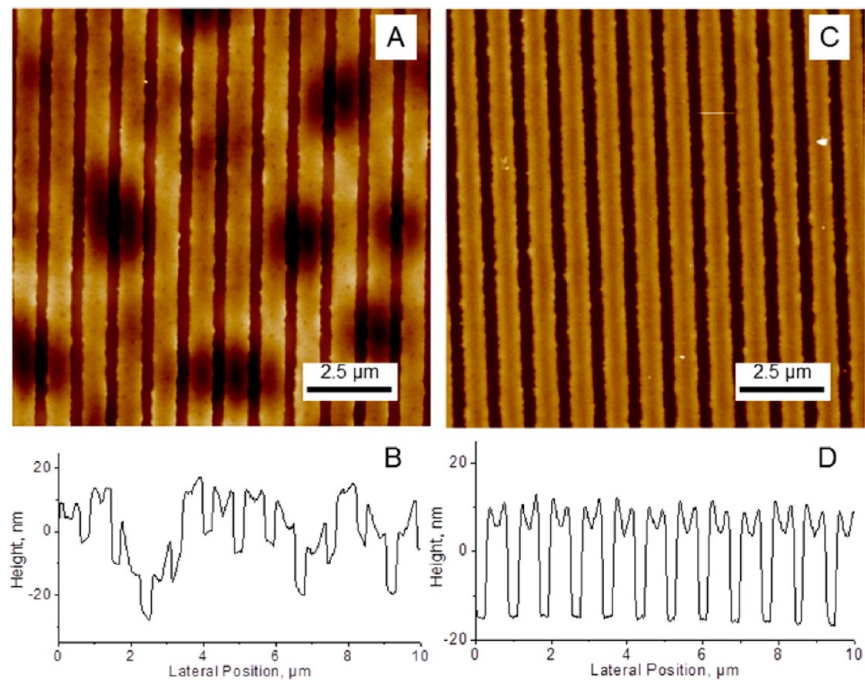


Figure 8. Sub-micrometer line pattern created via SAMIM of C16 films. AFM height (A) and representative cross-sectional profile (B) of SAMIM on C16 cast from HFIP. AFM height (C) and representative cross-sectional profile (D) of SAMIM on C16 cast from FA. Z scale: 60 nm.

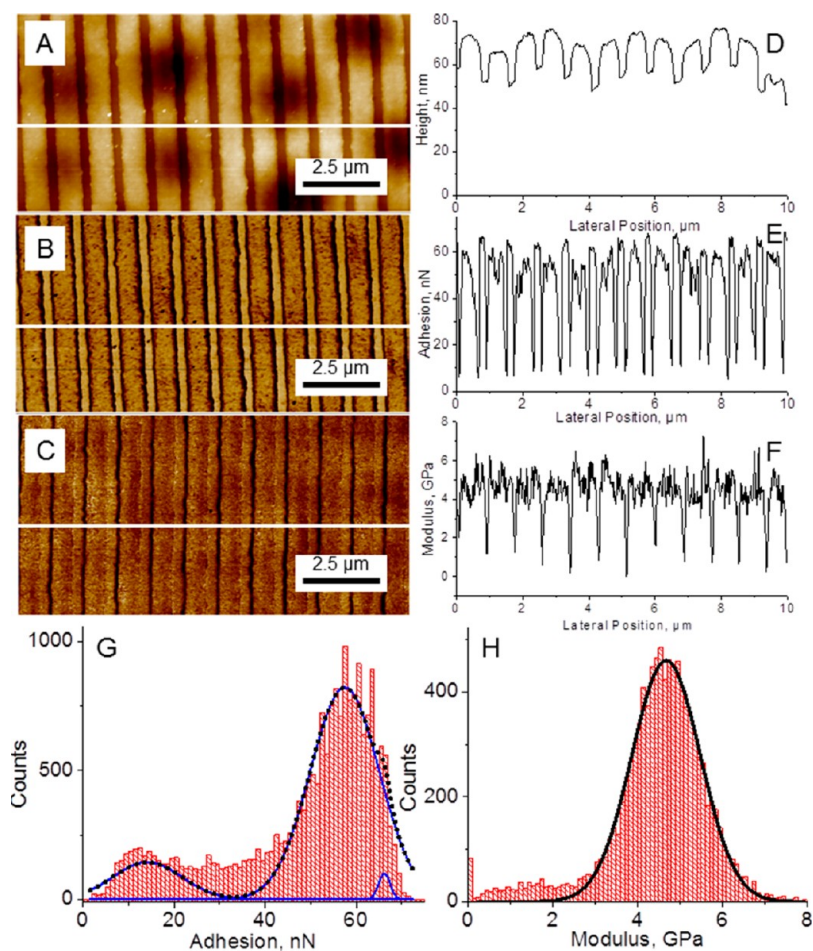


Figure 9. C16 cast from HFIP patterned via SAMIM. (A) Topography, (B) adhesion map, (C) modulus map. Representative cross sections: height (D), adhesion (E), and modulus (F). Histograms depicting the distribution of adhesion (G) and modulus (H) overlaid with Gaussian fits. Z scales: 60 nm, 90 nN, 9 GPa.

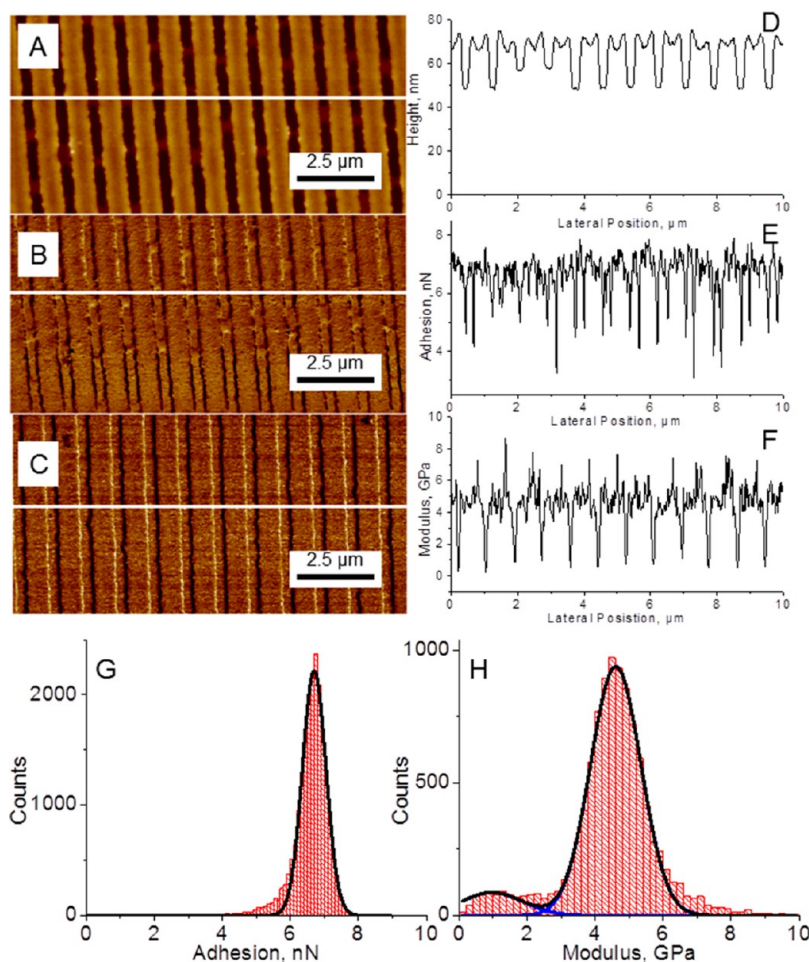


Figure 10. C16 cast from FA patterned via SAMIM. (A) Topography, (B) adhesion map, (C) modulus map. Representative cross sections: height (D), adhesion (E), and modulus (F). Histograms depicting the distribution of adhesion (G) and modulus (H) overlaid with Gaussian fits. Z scales: 60 nm, 4 nN, 9 GPa.

Micromapping of the SAMIM-patterned C16 film cast from HFIP shows the same contrast in surface adhesion as seen in the larger, square pattern (Figure 9), further confirming that the raised areas have been exposed to methanol, while the lower areas have not. The trimodal distribution is not as readily apparent in the histogram here, due to the smaller amount of untransformed regions, but deconvolution using three Gaussian curves resulted in peak centers located at 64 nN, 56 nN, and 10 nN, agreeing very well with the results presented above.

Also presented in Figure 9 is a surface distribution of the modulus data. Similar to the square pattern, there is no significant, regular contrast between the transformed and untransformed regions of the pattern. The modulus distribution profile shows an average modulus of 4.7 GPa, 2 times the average value of the square pattern. This apparent increase most likely is due to both the topographical contributions of the uneven sample surface as well as the different deformational levels in one force–distance cycle with identical parameters.

Figure 10 shows the adhesion and modulus data for C16 films cast from FA and patterned with sub-micrometer lines via SAMIM. According to the adhesion distribution shown in Figure 10G, the patterned film has an average adhesional attraction to the AFM tip of 6.7 nN, and lacks any significant contrast between the two regions. According to Figure 10H, the film has an average modulus of 4.6 GPa. Both of these values agree well with the data recorded from the square pattern of

C16 cast from FA. Also, the modulus of 4.6 GPa agrees well with the modulus of 4.7 GPa observed in the SAMIM pattern of C16 cast from HFIP.

CONCLUSIONS

In conclusion, we have demonstrated directed self-assembly to selectively pattern thin films of recombinant spider silk proteins. In comparison to our previous studies utilizing secondary structural features to pattern SF films, these patterned C16 films displayed much more complex behavior. As a result of the different mechanical properties intrinsic to the initial structure elements present in each film, which are influenced by the solvent from which the C16 thin films are cast, drastically different morphologies were observed. While a prominent feature in each pattern was tearing in unmasked regions of the C16 films, we did observe a strong interface between the transformed and untransformed regions without apparent crack propagation, which was a very common feature with regular patterned SF thin films. Finally, adding some complexity to our patterned films, we demonstrated using a different patterning technique, namely SAMIM, a successful increase of the resolution of our pattern feature sizes. More specifically, we have achieved precise patterning of protein secondary structure with modest vapor-based treatment that has submicrometer periodicity, a feature that to our knowledge has not yet been shown in the literature.

■ ASSOCIATED CONTENT

● Supporting Information

Supporting Information is available that includes additional discussion on the patterning process, the observed tearing observed in the patterned C16 films, the adhesion recorded in these experiments, as well as a note on the stability of the C16 solution. This material is available free of charge via the Internet at <http://pubs.acs.org>.

■ AUTHOR INFORMATION

Corresponding Author

*Tel.: 404-894-6081; Fax: 404-385-3112; E-mail address: vladimir@mse.gatech.edu.

Notes

The authors declare no competing financial interest.

■ ACKNOWLEDGMENTS

S.L.Y., M.G., and V.V.T. would like to acknowledge financial support from the Air Force Office of Scientific Research under AFOSR-FA9550-08-1-0446, FA9550-10-1-0172, and FA9550-09-1-0513 Grants, and V.V.T. thanks the Alexander von Humboldt Foundation for support of his stay at U. Bayreuth. A.F., M.G., and C.H. acknowledge support from the German Science foundation within the SFB840, TP B5 award. T.S. acknowledges support from German Science foundation within the SFB840, TP A8 award.

■ REFERENCES

- (1) Humenik, M.; Scheibel, T.; Smith, A. M. *Prog. Mol. Biol. Transl. Sci.* **2011**, *103*, 131–185.
- (2) Leal-Egaña, A.; Scheibel, T. *Biotechnol. Appl. Biochem.* **2010**, *55*, 155–167.
- (3) Eisoldt, L.; Smith, A.; Scheibel, T. *Mater. Today* **2001**, *14*, 80–86.
- (4) Vepari, C.; Kaplan, D. K. *Prog. Polym. Sci.* **2007**, *32*, 991–1007.
- (5) Vollrath, F. *Nature* **2010**, *466*, 319.
- (6) Jin, H.; Kaplan, D. K. *Nature* **2003**, *424*, 1057–1061.
- (7) Xu, M.; Lewis, R. V. *Proc. Natl. Acad. Sci. U.S.A.* **1990**, *87*, 7120–7124.
- (8) Buehler, M. J.; Yung, Y. C. *Nat. Mater.* **2009**, *8*, 175–188.
- (9) Lawrence, B. D.; Cronin-Golomb, M.; Georgakoudi, I.; Kaplan, D. L.; Omenetto, F. G. *Biomacromolecules* **2008**, *9*, 1214–1220.
- (10) Perry, H.; Gopinath, A.; Kaplan, D. L.; Dal Negro, L.; Omenetto, F. G. *Adv. Mater.* **2008**, *20*, 3070–3072.
- (11) Heim, M.; Römer, L.; Scheibel, T. *Chem. Soc. Rev.* **2010**, *39*, 156–164.
- (12) Hardy, J. G.; Römer, L. M.; Scheibel, T. R. *Polymer* **2008**, *49*, 4309–4327.
- (13) Altman, G. H.; Diaz, F.; Jakuba, C.; Calabro, T.; Horan, R. L.; Chen, J.; Lu, H.; Richmond, J.; Kaplan, D. L. *Biomaterials* **2003**, *24*, 401–416.
- (14) Heim, M.; Keerl, D.; Scheibel, T. *Angew. Chem., Int. Ed.* **2009**, *48*, 3584–3596.
- (15) Lewis, R. V. *Chem. Rev.* **2006**, *106*, 3762.
- (16) Shulha, H.; Foo, C. W. P.; Kaplan, D. L.; Tsukruk, V. V. *Polymer* **2006**, *47*, 5821–5830.
- (17) Kharlampieva, E.; Kozlovskaya, V.; Gunawidjaja, R.; Shevchenko, V. V.; Vaia, R.; Naik, R. R.; Kaplan, D. L.; Tsukruk, V. V. *Adv. Funct. Mater.* **2010**, *20*, 840–846.
- (18) Kharlampieva, E.; Kozlovskaya, V.; Wallet, B.; Shevchenko, V. V.; Naik, R. R.; Vaia, R.; Kaplan, D. L.; Tsukruk, V. V. *ACS Nano* **2010**, *4*, 7053–7063.
- (19) Greving, I.; Cai, M.; Vollrath, F. *Biomacromolecules* **2012**, *13*, 676–682.
- (20) Jiang, C.; Wang, X.; Gunawidjaja, R.; Lin, Y. -H.; Gupta, M. K.; Kaplan, D. L.; Naik, R. R.; Tsukruk, V. V. *Adv. Funct. Mater.* **2007**, *17*, 2229–2237.
- (21) Shchepelina, O.; Drachuk, I.; Gupta, M. K.; Lin, J.; Tsukruk, V. V. *Adv. Mater.* **2011**, *23*, 4655.
- (22) Elices, M.; Guinea, G. V.; Pérez-Rigueiro, J.; Plaza, G. R. *Mater. Sci. Eng., C* **2011**, *6*, 1184–1188.
- (23) Lotz, B.; Keith, H. D. *J. Mol. Biol.* **1971**, *61*, 201–202.
- (24) Takahashi, Y.; Gehoh, M.; Yuzuriha, K. *Int. J. Biol. Macromol.* **1999**, *24*, 127–138.
- (25) Römer, L.; Scheibel, T. *Prion* **2008**, *2*, 154–161.
- (26) Asakura, T.; Kuzuhara, A.; Tabeta, R.; Saito, H. *Macromolecules* **1985**, *18*, 1841–1845.
- (27) Wang, X.; Kim, H. -J.; Xu, P.; Matsumoto, A.; Kaplan, D. L. *Langmuir* **2005**, *25*, 11335–11341.
- (28) Kharlampieva, E.; Zimmitsky, D.; Gupta, M.; Bergman, K. N.; Kaplan, D. L.; Naik, R. R.; Tsukruk, V. V. *Chem. Mater.* **2009**, *21*, 2696–2704.
- (29) Gupta, M. K.; Singamaneni, S.; McConney, M.; Drummy, L. F.; Naik, R. R.; Tsukruk, V. V. *Adv. Mater.* **2010**, *22*, 115–119.
- (30) Lefèvre, T.; Rousseau, M. -E.; Pérolet, M. *Biophys. J.* **2007**, *92*, 2885–2895.
- (31) Metwalli, E.; Slotta, U.; Darko, C.; Roth, S. V.; Scheibel, T.; Papadakis, C. M. *Appl. Phys. A: Mater. Sci. Process.* **2007**, *89*, 655–661.
- (32) Humenik, M.; Smith, A. M.; Scheibel, T. *Polymers* **2011**, *3*, 640–661.
- (33) Vendrely, C.; Scheibel, T. *Macromol. Biosci.* **2007**, *7*, 401–409.
- (34) Huemmerich, D.; Helsen, C. W.; Quedzuweit, S.; Oschmann, J.; Rudolph, R.; Scheibel, T. *Biochemistry* **2004**, *43*, 13604–13612.
- (35) Heim, M.; Römer, L.; Scheibel, T. *Chem. Soc. Rev.* **2009**, *39*, 156–164.
- (36) Hirota, N.; Mizuno, K.; Goto, Y. *Protein Sci.* **1997**, *6*, 416–421.
- (37) Um, I. C.; Kweon, H. Y.; Park, Y. H. *Int. J. Biol. Macromol.* **2001**, *29*, 91–97.
- (38) Ha, S. -W.; Tonelli, A. E.; Hudson, S. *Biomacromolecules* **2005**, *6*, 1722–1731.
- (39) Zhao, C.; Yao, J.; Masuda, H.; Kishore, R.; Asakura, T. *Biopolymers* **2003**, *69*, 253–259.
- (40) Trabbic, K. A.; Yager, P. *Macromolecules* **1998**, *31*, 462–471.
- (41) Spiess, K.; Ene, R.; Keenan, C. D.; Senker, J.; Kremer, F.; Scheibel, T. *J. Mater. Chem.* **2011**, *21*, 13594–13604.
- (42) Ko, H.; Jiang, C.; Tsukruk, V. V. *Chem. Mater.* **2005**, *17*, 5489–5497.
- (43) Kim, E.; Xia, Y.; Zhao, X. -M.; Whitesides, G. M. *Adv. Mater.* **1997**, *9*, 651–654.
- (44) Qin, D.; Xia, Y.; Whitesides, G. M. *Nat. Protoc.* **2010**, *5*, 491–502.
- (45) McConney, M. E.; Singamaneni, S.; Tsukruk, V. V. *Polym. Rev.* **2010**, *50*, 235–286.
- (46) Derjaguin, B. V.; Muller, V. M.; Toporov, Y. P. *J. Colloid Interface Sci.* **1975**, *53*, 314–326.
- (47) Tsukruk, V. V.; Singamaneni, S. *Scanning Probe Microscopy of Soft Matter: Fundamentals and Practices*; Wiley-VCH: Weinheim, Germany, 2012; p 661.
- (48) He, W. -Z.; Newell, W. R.; Haris, P. I.; Chapman, D.; Barber, J. *Biochemistry* **1991**, *30*, 4552–4559.
- (49) Hertzberg, R. W. *Deformation and Fracture Mechanics of Engineering Materials*, 4th ed; John Wiley & Sons: New York, 1996.
- (50) Spiess, K.; Ene, R.; Keenan, C. D.; Senker, J.; Kremer, F.; Scheibel, T. *J. Mater. Chem.* **2011**, *21*, 13594–13604.
- (51) Best, R. B.; Chen, Y. -G.; Hummer, G. *Structure* **2005**, *13*, 1755–1763.
- (52) Chan, H. S.; Dill, K. A. *J. Chem. Phys.* **1994**, *100*, 9238–9257.
- (53) Travasso, R. D. M.; Faísca, P. F. N.; Rey, A. *J. Chem. Phys.* **2010**, *133*, 125102-1–125102-9.
- (54) Junier, I.; Ritort, F. *AIP Conf. Proc.* **2006**, *851*, 70–95.